

PETE'S THESIS

by

Peter Thompson

A thesis submitted in conformity with the requirements
for the degree of Doctor of Philosophy
Graduate Department of Physics
University of Toronto

Copyright © 2011 by Peter Thompson

Abstract

Pete's Thesis

Peter Thompson

Doctor of Philosophy

Graduate Department of Physics

University of Toronto

2011

(At most 150 words for M.Sc. or 350 words for Ph.D.)

Contents

1	Testbeam Results	1
1.1	Event Selection	1
1.2	Electron analysis	3
1.2.1	Cylindrically Clustered Results	3
1.2.2	Hadron Results	15
1.3	Topologically Clustered Results	24
1.3.1	Electrons	24
1.3.2	Hadrons	28
1.3.3	Cluster moments	33
	Bibliography	37

Chapter 1

Testbeam Results

1.1 Event Selection

The three scintillators located on the adjustable table (S1, S2, S3) are used for triggering. Coincident signals are required from all three in order for the event to be accepted. Signal from the veto counter indicates that the beam particle has scattered off the upstream material, and in these cases the event is rejected. For data taken from an electron beam, events were also rejected if there was any signal in either the tail-catcher or the muon counter, indicating the presence of muons. Muons can sometimes be produced during hadronic showers, and so these cuts were not applied for data taken from pion beams.

A series of “Beam Cleaning” cuts were applied, which also used information from the scintillators. The beam cleaning cuts were implemented in order to remove events which contained multiple beam particles and events in which the beam particle had scattered off the upstream material. In order to remove events in which multiple particles were present, the signal from each scintillator was compared to that expected for a minimum ionizing particle (MIP). If a single scintillator produced a signal consistent with 5 times that of a MIP, or at least two scintillators gave signals over twice the MIP threshold, the event was rejected.

Particle tracks are reconstructed by performing a linear fit on the data from the BPCs. The $x - z$ and $y - z$ planes are fitted separately, with the BPCs providing six measurements of the track in each plane. If the χ^2 value for either fit exceeds 40.0, the event is rejected. These tracks were then used to make “beam envelope” cuts, which were intended to remove events containing undesired particles. The secondary beams delivered to the testing area were not completely pure, and so hadrons were sometimes present in the electron beams and protons sometimes present in the pion beams. The magnet systems in the H6 beamline tended to place electrons and hadrons into different areas of phase space, due to differences in their charge to mass ratios. The x intercept of the track, c_x , is measured using the BPC closest to the FCal. This is used to determine an “ideal” slope in the $x - z$ plane for the desired particle type, $m_{x,i}(c_x)$, as well as a width parameter, $\sigma_x(c_x)$. The procedure is then repeated to obtain the intercept, ideal slope, and width parameter in the $y - z$ plane, denoted as c_y , $m_{y,i}(c_y)$, and $\sigma_y(c_y)$ respectively. The quantity

$$\Delta S = \left(\left(\frac{m_{x,i}(c_x) - m_{x,m}}{\sigma_x(c_x)} \right)^2 + \left(\frac{m_{y,i}(c_y) - m_{y,m}}{\sigma_y(c_y)} \right)^2 \right)^{1/2} \quad (1.1)$$

is then calculated, where $m_{x,m}$ and $m_{y,m}$ are the measured track slopes in the x and y directions, respectively. If ΔS exceeds a specified threshold (1.25 in this analysis), the measured track is deemed to lie outside the beam envelope for the desired particle type, and the event is rejected.

While the primary purpose of the BPCs was to obtain tracking information on the beam particles, they were used in the beam cleaning in a similar way to the scintillators. A key feature of MWPCs is that the total charge arriving at an anode is proportional to the total number of electron-ion pairs produced in the chamber, and from this the number of ionizing particles that passed through the active areas could be inferred. Events were rejected if a single BPC produced a signal five times greater than that expected for a

single MIP, or if at least two BPCs generated a signal twice that expected for a single MIP.

As mentioned earlier, two TDCs were used to measure the time interval from the trigger signal until the clock pulse on the TTC, at which time the signals from the calorimeter were sampled. output from the TDC is given as an integer number of TDC counts, between ~ 300 and ~ 800 , which covers a time interval of 25 ns and thus gives the TDC a time resolution of 50 ps. There are three regions where a mismeasurement of the TDC can be problematic: near the TDC's minimum value, its maximum value, and the "wrap around" region. The wrap around point is where the phase jump occurs, such that the time interval measured by the TDC jumps suddenly from 0 ns to 25 ns. The TDC phase quality is defined as the smallest difference between the TDC reading and one of the problematic values. Event timing was determined using the TDC which had the highest phase quality. The event was rejected if the TDC phase quality did not lie in the range $20 < \text{TDCPhaseQuality} < 230$, as in these cases the better clock choice was still within 1 ns of a problematic region.

The CEDAR detector was also used to improve the beam purity. This was mainly used to eliminate proton events when taking data with π^+ beams, by rejecting events containing beam particles that the CEDAR did not identify as charged pions. However, the CEDAR was also used when recording electron data at 60 GeV, as it proved exceptionally difficult to obtain a relatively pure electron beam at this energy.

1.2 Electron analysis

1.2.1 Cylindrically Clustered Results

Using the tracking information obtained from the BPCs, the point at which the beam particles strike the front face of the calorimeter can be determined. Cylindrical clusters are then formed by summing the energy of each cell within a certain radius of this

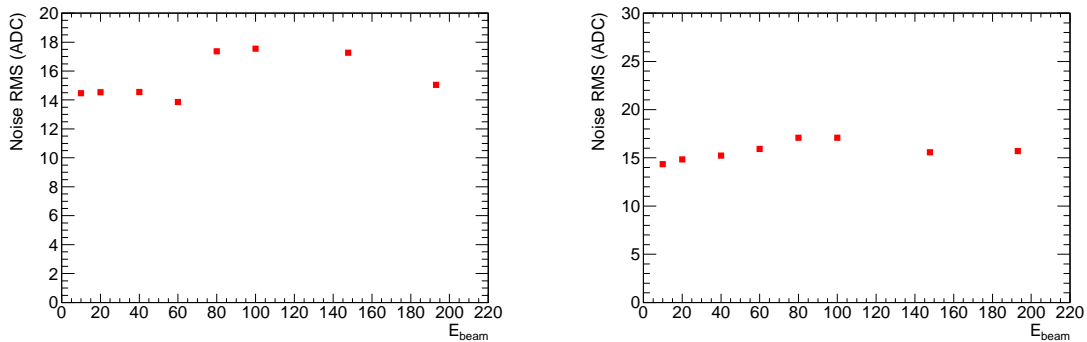


Figure 1.1: RMS of the electronics noise clustered at different energies, for beams directed at position 4L (left) and position 4H (right).

impact point. A clustering radius of 8 cm is used for analysis of the electron data. For electromagnetic showers, about 80-90% of the energy is contained within a cylinder of radius ρ_M , the Molière radius. The Molière radius in FCal1 is 17mm, and so about 99% of the shower's energy should be contained within an 8 cm cluster. Clusters with radii 12 cm and 16 cm are also generated during reconstruction. These larger clusters capture about 1% more energy than the 8 cm cluster, however the noise contained within the cluster increases by $\sim 50\%$ at a radius of 12 cm and $\sim 100\%$ at a radius of 16 cm. For this reason 8 cm clusters are used in the analysis of electron data.

The energy reconstructed for a given particle is dependent on the position at which that particle impacts the calorimeter, as an electron striking the centre of an electrode rod will deposit less visible energy in the calorimeter than one that impacts close to the liquid argon gap. As the diameter of the beamspot (65 mm) is an order of magnitude larger than the spacing between adjacent electrodes (7.5 mm in FCal1), many different impact points are sampled, which leads to a non-gaussian distribution in the response. A good fit to the data is obtained using a double gaussian function,

$$F(E) = A_1 \exp\left(-\frac{(E - \mu_1)^2}{2\sigma_1^2}\right) + A_2 \exp\left(-\frac{(E - \mu_2)^2}{2\sigma_2^2}\right) \quad (1.2)$$

where A_i , μ_i , and σ_i are the peaks, means and widths of the component gaussians. The

mean response (\bar{E}) is taken as the first moment of $F(E)$, where the i -th moment is given by

$$\mu_i = \frac{\int_{E_{\min}}^{E_{\max}} E^i F(E) dE}{\int_{E_{\min}}^{E_{\max}} F(E) dE}, \quad (1.3)$$

where E_{\min} and E_{\max} are values obtained the histogram of the energy response. The lower limit, E_{\min} , is taken from the low edge of the lowest energy bin energy bin that is not empty, while E_{\max} is the upper edge of the highest non-empty histogram bin. The width, σ , is determined from the second moment, such that

$$\sigma = (\mu_2 - \mu_1^2)^{1/2}. \quad (1.4)$$

Statistical uncertainties on these quantities may be written in terms of higher order moments. For simplicity, a (single) gaussian fit is made to the response, and the moments of this gaussian are used to compute the statistical uncertainties. This procedure yields

$$\Delta \bar{E} = \Delta \mu_1 = \frac{\sigma_g}{\sqrt{N_g}} \quad (1.5)$$

$$\Delta \sigma = \frac{\sigma_g}{\sqrt{2N_g}}, \quad (1.6)$$

where σ_g is the width of the gaussian and N_g is the number of events contained within it (i.e. its integral).

The response of the FCal to electron beams is plotted in figures 1.2 and 1.3, for beams directed at position 4L and 4H respectively. These results are summarized in tables 1.1 and 1.2. The properties of noise are obtained by reconstructing randomly triggered events. For each physics event, a randomly triggered event taken from the same run is chosen at random and reconstructed. The beam impact point from the physics event is used in the randomly triggered event, and a cylindrical cluster is formed around this point. A gaussian fit is then performed on the clustered energies, and the width of this is used as an estimate of the noise present in the physics events. This width is used in

the computation of the energy resolution, which is described below.

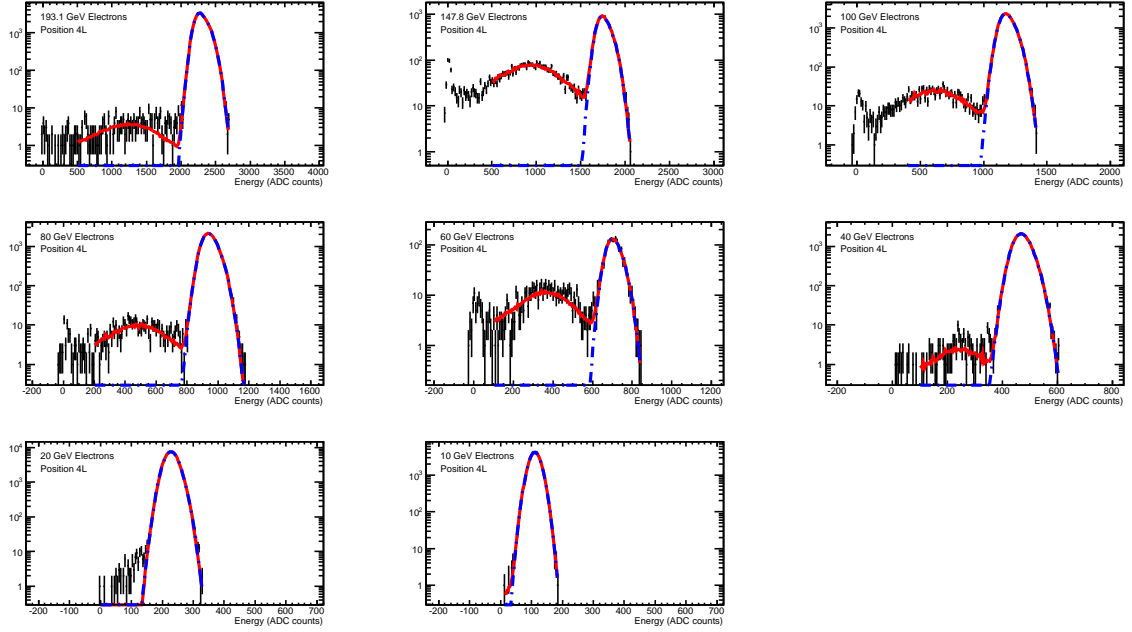


Figure 1.2: Response of the FCal to electron beams directed at position 4L. The blue dashed curve double gaussian fit to the electron peak, while the red curve shows the total fit to the electron peak plus the contaminant hadron contribution.

Beam Energy (GeV)	Fitted Mean (ADC)	Fitted Width (ADC)	Noise (ADC)
193.1 GeV	2300.6 ± 0.5	94.4 ± 0.3	15.1 ± 0.1
147.8 GeV	1763.4 ± 0.8	75.9 ± 0.5	17.2 ± 0.1
100 GeV	1186.4 ± 0.3	56.8 ± 0.2	17.5 ± 0.1
80 GeV	946.9 ± 0.3	47.9 ± 0.2	17.4 ± 0.1
60 GeV	708.1 ± 0.9	36.6 ± 0.7	13.9 ± 0.2
40 GeV	472.4 ± 0.2	29.9 ± 0.1	14.6 ± 0.1
20 GeV	229.3 ± 0.1	21.7 ± 0.1	14.5 ± 0.0
10 GeV	110.9 ± 0.1	17.7 ± 0.1	14.5 ± 0.1

Table 1.1: Results for the FCal response to electrons, directed at position 4L. Quoted errors are statistical only.

The simulated response to electrons is shown in figure 1.4 for position 4L and figure 1.5 for position 4H, and these results are summarized in tables 1.3 and 1.4. All of the physics lists listed in section ?? model electromagnetic showers in the same way, and so

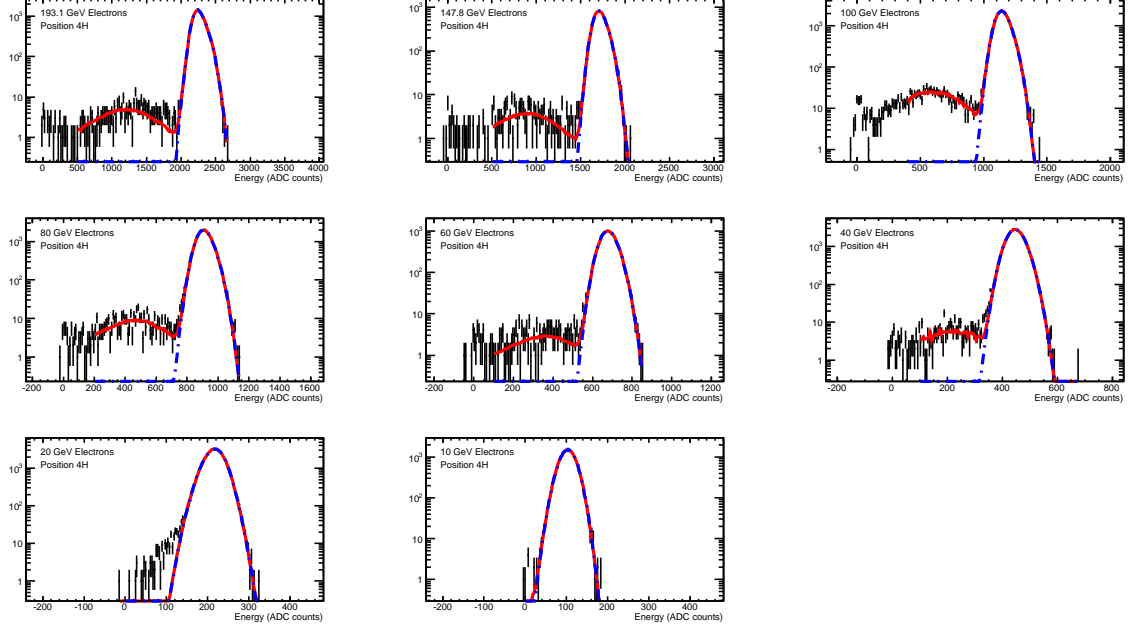


Figure 1.3: Response of the FCal to electron beams directed at position 4H. The blue dashed curve double gaussian fit to the electron peak, while the red curve shows the total fit to the electron peak plus the contaminant hadron contribution.

Beam Energy (GeV)	Fitted Mean (ADC)	Fitted Width (ADC)	Noise (ADC)
193.1 GeV	2263.9 ± 0.7	90.9 ± 0.5	15.7 ± 0.1
147.8 GeV	1718.3 ± 0.8	72.1 ± 0.5	15.6 ± 0.1
100 GeV	1150.8 ± 0.3	55.1 ± 0.2	17.1 ± 0.1
80 GeV	912.1 ± 0.3	48.8 ± 0.2	17.1 ± 0.1
60 GeV	680.1 ± 0.4	40.5 ± 0.2	15.9 ± 0.1
40 GeV	448.1 ± 0.2	30.9 ± 0.1	15.2 ± 0.1
20 GeV	215.8 ± 0.1	23.1 ± 0.1	14.9 ± 0.0
10 GeV	102.7 ± 0.1	18.5 ± 0.1	14.3 ± 0.1

Table 1.2: Results for the FCal response to electrons, directed at position 4H. Quoted errors are statistical only.

no distinction among physics lists is made for the Monte Carlo results contained in this section.

The double gaussian fit is performed on the electron peak in the response distribution. While the beam envelope cuts improve the purity of the electron sample, some of these

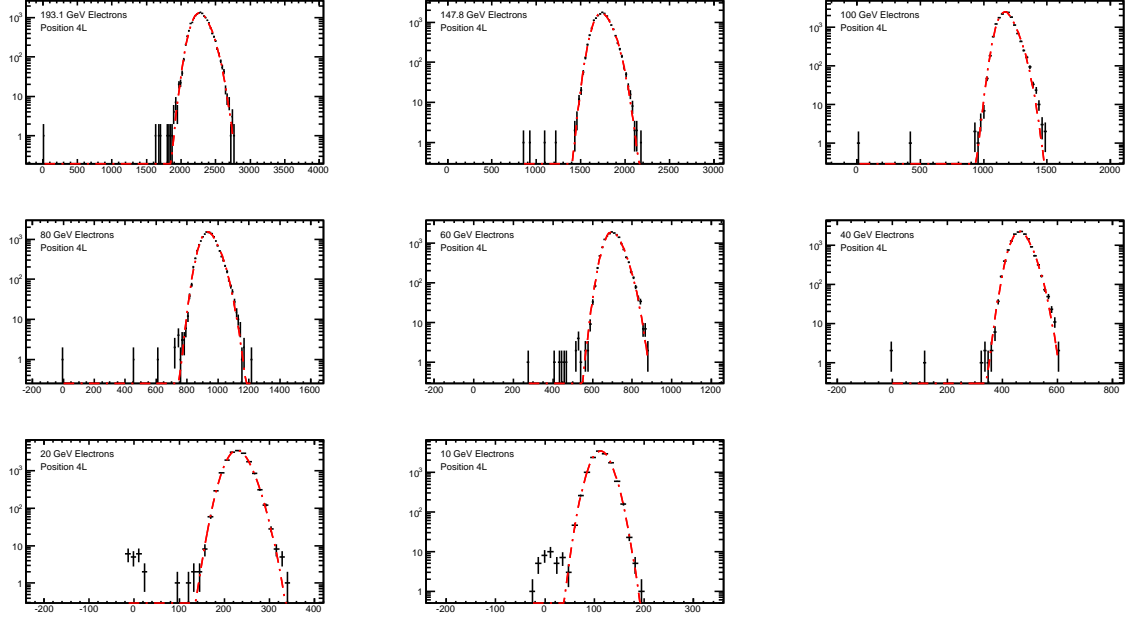


Figure 1.4: Monte Carlo results for electron beams directed at position 4L.

Beam Energy (GeV)	Fitted Mean (ADC)	Fitted Width (ADC)	Noise (ADC)
193.1 GeV	2285.2 ± 0.9	114.3 ± 0.7	14.2 ± 0.1
147.8 GeV	1747.4 ± 0.7	91.3 ± 0.5	17.0 ± 0.1
100 GeV	1180.2 ± 0.5	62.5 ± 0.3	17.4 ± 0.1
80 GeV	942.8 ± 0.4	51.7 ± 0.3	14.1 ± 0.1
60 GeV	705.3 ± 0.3	40.9 ± 0.2	14.2 ± 0.1
40 GeV	467.9 ± 0.3	31.6 ± 0.2	14.5 ± 0.1
20 GeV	230.5 ± 0.2	22.2 ± 0.1	14.3 ± 0.1
10 GeV	112.5 ± 0.2	18.0 ± 0.1	14.3 ± 0.1
5 GeV	53.1 ± 0.1	16.9 ± 0.1	14.1 ± 0.1

Table 1.3: Simulated response of the FCal to electron beams directed at position 4L. Quoted uncertainties are statistical only.

events still contain showers initiated by hadrons. The high tail of the hadron distribution overlaps with the low tail of the electron peak, and this effect must be accounted for when analysing the data. This is accomplished by including data taken from hadron runs into the fit for the electron response. The total function fitted to the distributions shown in figure 1.2 is given by

$$G(E) = F(E) + w H_{\pi}(E), \quad (1.7)$$

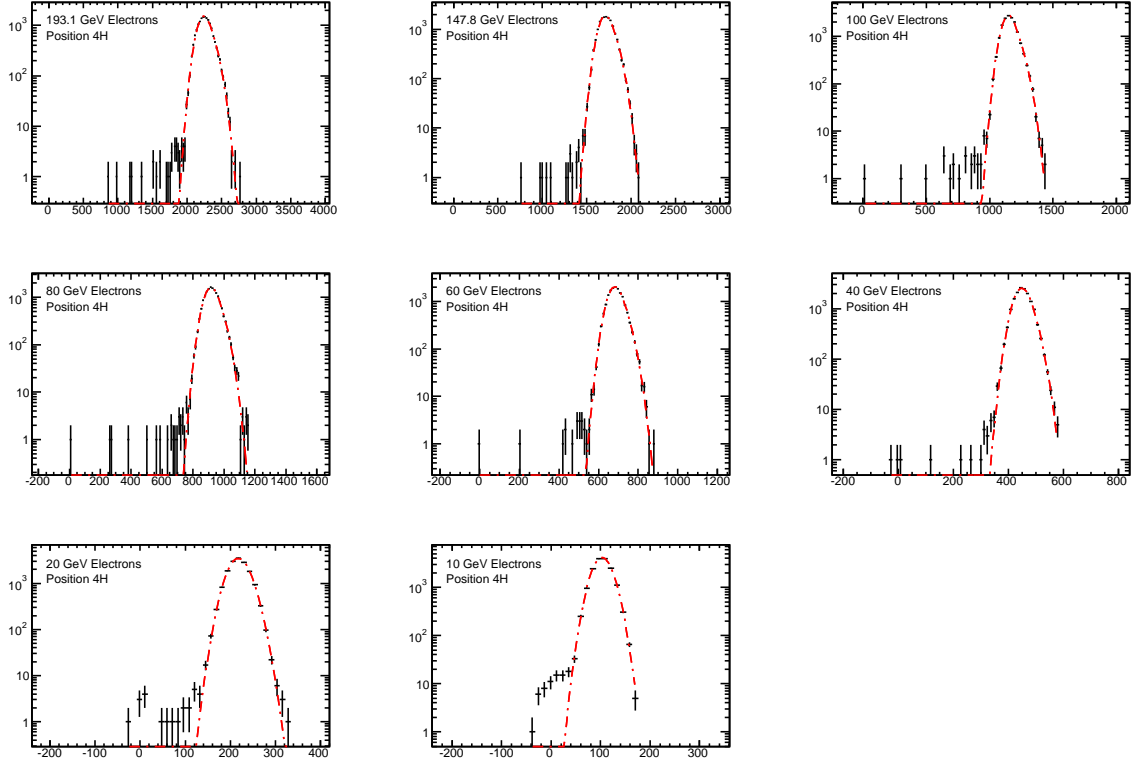


Figure 1.5: Monte Carlo results for electron beams directed at position 4H.

Beam Energy (GeV)	Fitted Mean (ADC)	Fitted Width (ADC)	Noise (ADC)
193.1 GeV	2259.7 ± 0.8	103.2 ± 0.6	15.9 ± 0.1
147.8 GeV	1723.5 ± 0.7	82.8 ± 0.5	15.6 ± 0.1
100 GeV	1159.5 ± 0.4	58.4 ± 0.3	17.0 ± 0.1
80 GeV	923.0 ± 0.4	48.2 ± 0.3	17.1 ± 0.1
60 GeV	687.7 ± 0.3	39.3 ± 0.2	16.1 ± 0.1
40 GeV	452.4 ± 0.2	30.7 ± 0.2	15.0 ± 0.1
20 GeV	218.8 ± 0.2	22.3 ± 0.1	14.6 ± 0.1
10 GeV	103.5 ± 0.1	18.4 ± 0.1	14.3 ± 0.1

Table 1.4: Simulated response of the FCal to electron beams directed at position 4H. Quoted uncertainties are statistical only.

where $F(E)$ is the double gaussian function described above. The “function” $H_\pi(E)$ is derived from data taken during pion runs. Cylindrical clusters with radius 8 cm are formed for each pion event, and used to fill a histogram with the same binning as is used for the electron response. The energy E is then converted to a bin number, and

the number of entries in this bin is taken as the value of $H_\pi(E)$. The parameter w corresponds to a weight for the hadron data and is allowed to freely vary in the fitting, as are the parameters of the double gaussian.

The two dominant sources of systematic uncertainties arise from the cluster radius and the beam polarity. The electron beams used in this study were secondary or tertiary beams produced by directing proton beams from the SPS at a fixed target. At higher energies a secondary beam was used, the polarity of which ($e+$ or $e-$) was determined based on the needs of other neighboring experiments. At lower energies a tertiary beam was used, and the polarity of this beam could be chosen freely.

Data was taken at position 4L using both $e-$ and $e+$ beams at energies of 10 GeV and 20 GeV. Physically, electromagnetic showers induced by electrons should on average deposit the same energy as those initiated by positrons. The 10 GeV and 20 GeV results in figure 1.2 use data obtained from both $e+$ and $e-$ beams. Considered separately, the response to 10 GeV positrons is on average 1.6% higher than the response to electrons. At 20 GeV, the response to positrons is 1.0% higher than the response to electrons. This difference in response is attributed to variation in the beam conditions, and is considered as a source of systematic uncertainty.

As mentioned above, a larger clustering radius captures a slightly larger fraction of the showering particles energy, while significantly increasing the amount of noise present in the cluster. The choice of clustering radius is thus taken as a source of systematic uncertainty. Other systematic effects considered include the binning used in histograms, inclusion of the pion response in the electron fit, the parameterization used for the fit, and event selection criteria.

Linearity plots are shown in figures 1.6(a) (for position 4L) and 1.6(b) (position 4H), depicting the mean reconstructed energy as a function of beam energy. A linear fit has been applied to the plots, the results of which are given in table 1.12. The y intercept of the line was not fixed at zero when performing the fit, and was instead allowed to vary.

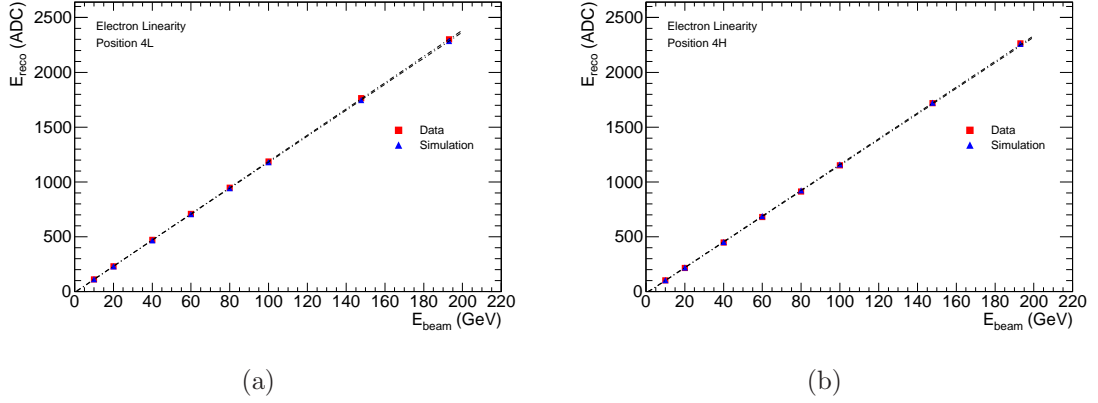


Figure 1.6: Linearity of the response to electrons at position 4L (left) and 4H (right).

linearity result	slope (ADC/GeV)	Intercept (ADC)
Data (4L)	11.964 ± 0.002	-9.26 ± 0.07
Simulation (4L)	11.865 ± 0.003	-6.45 ± 0.13
Data (4H)	11.693 ± 0.002	-17.53 ± 0.10
Simulation (4H)	11.747 ± 0.003	-15.44 ± 0.13

Table 1.5: Linearity results for electron data. quoted uncertainties are statistical.

The negative result for the intercept is due to energy losses in the upstream material, with the additional material at 4H giving an intercept larger in magnitude than that at 4L. As the simulation only modeled the beamline downstream of the B9 magnet, energy losses in materials upstream of this point would not be reflected in the simulation results. This is a possible explanation as to why the simulation results have a higher (less negative) intercept than those obtained from data.

The linearity shown in figure 1.6(a) uses events from both e^+ and e^- runs at 10 GeV and 20 GeV, which is considered to be the "nominal" case. The systematic uncertainty on the linearity due to beam polarity effects is obtained by varying the data used at 10 GeV and 20 GeV. At each of each of these energies, the response may be determined using events from e^+ runs, events from e^- runs, or events from either e^+ or e^- runs. A fit to the linearity is performed for each of these cases, and compared to the nominal result. The largest difference observed for each parameter is taken as the systematic uncertainty

due to beam polarity effects. At position 4H, only a single beam polarity was used at each energy, with e^+ beams being used at 10 GeV and 20 GeV. To obtain the uncertainty due to beam effects the responses at these points was scaled by the $e^+:e^-$ response ratio observed at 4L, in order to estimate the response to e^- beams. This yielded four different response combinations, which were then used to estimate the systematic uncertainty.

Other sources of systematic were treated in a similar fashion. For example, the effect of the cluster radius was estimated by using 12cm and 16cm clusters. A fit was performed on the resulting linearity plots, and the fit parameters were compared to those obtained using 8 cm clusters, with the largest difference taken as the uncertainty on that parameter. Systematic uncertainties from different sources were then summed in quadrature to obtain the final uncertainty on the results.

The linearity at position 4L is best described by a line with slope $12.0 \pm 0.1 \text{ ADC/GeV}$ and intercept -9.3 ± 1.1 ADC counts, where the quoted uncertainties are due to systematic effects. At position 4H, the linearity is described by a line with slope $11.7 \pm 0.2 \text{ ADC/GeV}$ and intercept -17.5 ± 1.6 ADC counts. A prediction of the ADC2GeV calibration factor was made prior to the beam test, based on a simulation of the FCal electronics chain and knowledge of the FCal geometry. The predicted value for FCal1 was found to be 12.0 ADC/GeV [?], in good agreement with the results obtained here.

The residuals obtained from the linearity fits are plotted in figure ???. Systematic uncertainties on the residuals were estimated using the method described above. When performing a fit on the data, the difference between the resulting set of residuals and the nominal residuals is taken as the uncertainty on the residuals due to that particular source of systematic error. The uncertainties from different sources are then summed in quadrature. From the plot in figure ??, it can be seen that the response at position 4L is linear to within 1%. This is also the case at position 4H for energies of 20 GeV and above.

The energy resolution of the FCal to electrons is plotted in figure 1.8. As the randomly

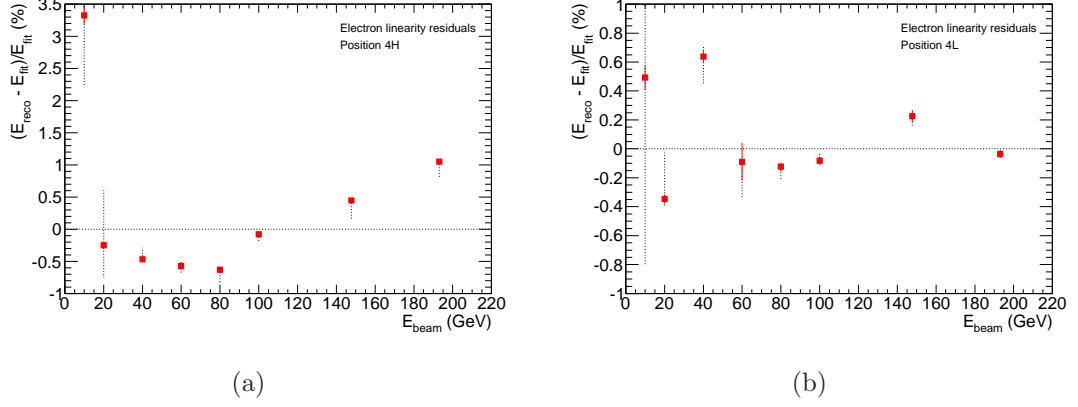


Figure 1.7: Residuals obtained from the linearity fit for electrons at position 4L (left) and 4H (right). Solid lines in the error bars represent the statistical uncertainties, while the systematic uncertainties are represented by the dotted lines.

triggered events provide information on the amount of noise present in the electronics, the contribution of this noise has been subtracted in quadrature from the width of the response. The resolution is thus defined as σ_E/\overline{E} , where

$$\sigma_E = \sqrt{\sigma^2 - \sigma_N^2} \quad (1.8)$$

where σ_N is the width of the noise distribution obtained from randomly triggered events and σ is the width of the response. The width, σ , is obtained from the double gaussian fit as described by equation 1.4, and the obtained values are listed in tables 1.1 and 1.2.

The resolution is fit to a function of the form

$$\frac{\sigma_E}{E} = \left(\frac{A^2}{E/\text{GeV}} + B^2 \right)^{\frac{1}{2}}, \quad (1.9)$$

where A is called the stochastic term, and represents the contribution to the resolution arising from fluctuations in the energy deposited in the liquid argon gaps of the FCal. The constant term, B , is due to energy independent effects on the resolution, such as non-uniformities in the calorimeter structure. A term proportional to E^{-2} is sometimes

included in equation 1.9 to describe the effects of noise on the resolution. As the noise has been accounted for by the subtraction procedure described above, this term has been omitted. The fit results are listed in table 1.6.

	Stochastic Term (% $\text{GeV}^{1/2}$)	Constant Term (%)
Data (4L)	27.0 ± 0.2	3.58 ± 0.02
Simulation (4L)	24.7 ± 0.3	4.56 ± 0.03
Data (4H)	33.7 ± 0.2	3.11 ± 0.03
Simulation (4H)	28.1 ± 0.3	3.96 ± 0.03

Table 1.6: Fit parameters for energy resolution to electrons. Quoted uncertainties are statistical only.

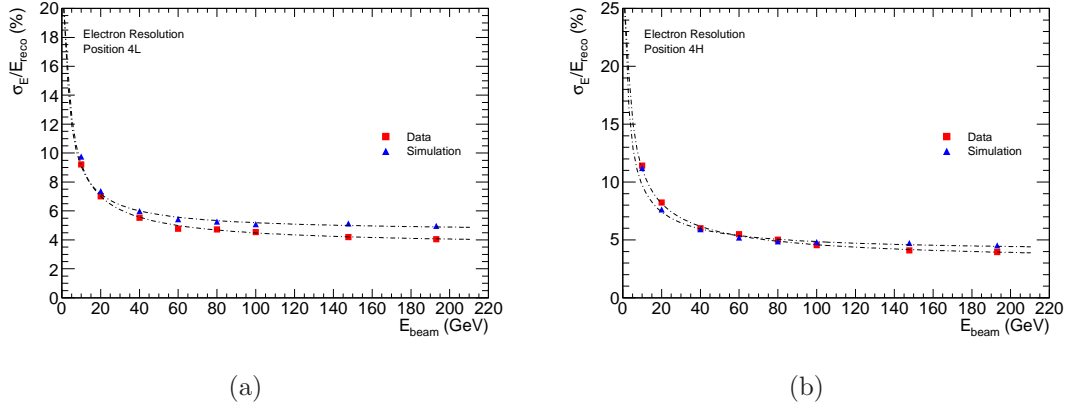


Figure 1.8: Energy resolution of the FCal to electrons, using data taken from position 4L (left) and 4H (right). A noise subtraction procedure has been applied, as described in the text.

The non-uniformity of the response with respect to the beam particles impact point on the calorimeter forms the dominant contribution to the constant term in the resolution. The additional upstream material present for runs directed at position 4H causes the beam particles to begin showering earlier. The energy in the shower is thus distributed over a larger area by the time it reaches the FCal, decreasing the impact point dependence and resulting in a lower constant term for the resolution measured at position 4H. The simulation results for electrons give a lower (i.e. better) resolution than that seen in data, although the discrepancy is smaller at position 4H than 4L.

1.2.2 Hadron Results

In the analysis of hadron data, the signal from the FCal is first calibrated to the electromagnetic (EM) scale. This is done by applying ADC2MeV factors, which convert the reconstructed pulse peak (in ADC counts) to the corresponding energy that would be deposited in the calorimeter by an electromagnetic particle (i.e. an electron or photon). The ADC2MeV values used in the reconstruction are 83.3 MeV/ADC, 163.9 MeV/ADC and 185.2 MeV/ADC for FCal1, FCal2 and FCal3 respectively, and were obtained from a SPICE simulation of the FCal electronics. As discussed above, the predicted value for FCal1 is in good agreement with the value obtained from the linearity of the FCal1 response to electrons. Data taken in a previous beam test allowed the ratio of the FCal1 and FCal2 responses to be studied, and the SPICE results agree with this data to within 5%.

Figure 1.9 shows the transverse distribution of energy (at the EM scale) for 200 GeV hadrons showering within the FCal. Figures 1.9(a) and 1.9(c) show the energy deposited within a transverse distance r from the impact point, as a fraction of the energy deposited within 21cm of the impact point. Figures 1.9(b) and 1.9(d) show the derivatives of these functions. The Monte Carlo results (for all physics lists studied) show that a larger fraction of the energy is contained within smaller transverse distances, indicating that the simulated showers are smaller than those observed in data.

Cylindrical clusters with radius 16cm are used for analysis of the hadron data. The longitudinal shower profiles for 200 GeV hadrons are shown in figure 1.11. These show the amount of energy (at the EM scale) clustered within each module as a fraction of the total energy clustered in all modules. The Monte Carlo results deposit more energy in FCal1 and less energy in FCal2, indicating the the simulated showers are shorter than those observed in data. The shower maximum is the point at which the particle shower contains the largest number of particles, and thus corresponds to the depth at which the rate of energy deposition is greatest. The additional material in front of position 4H

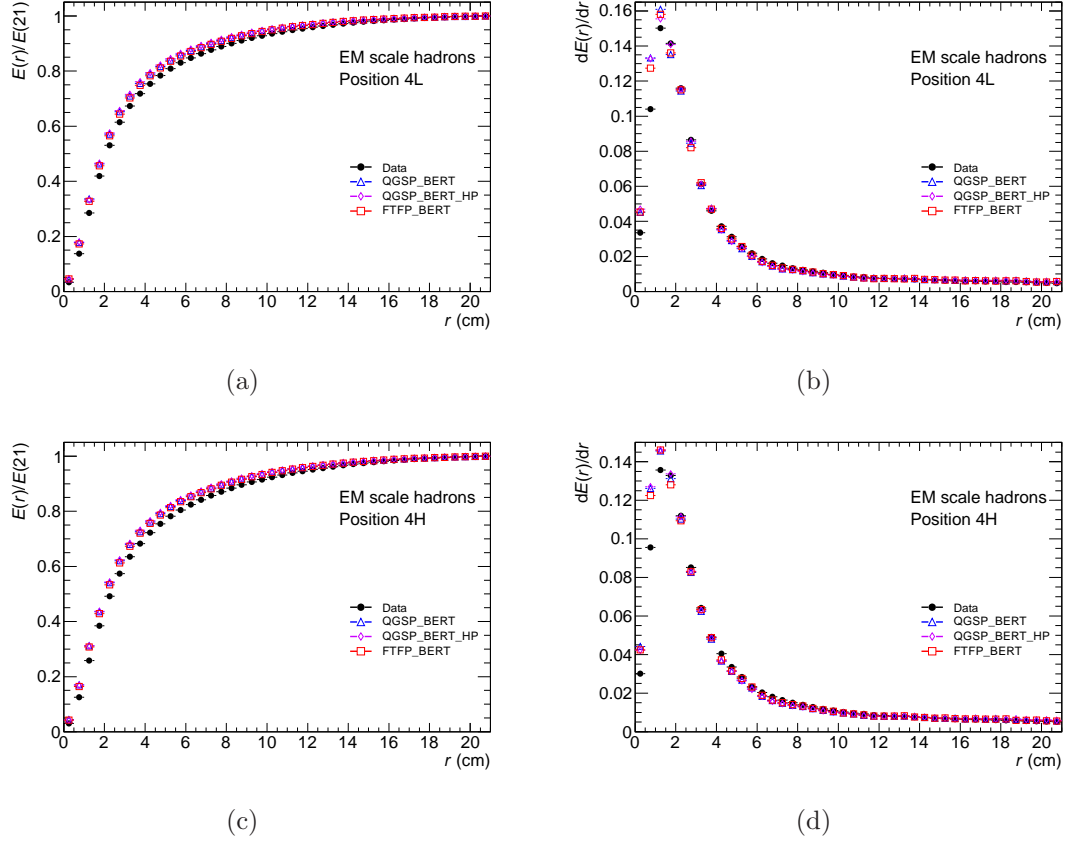


Figure 1.9: Energy distribution within the FCal as a function of the transverse distance (r) from the projected beam impact point. Results obtained from position 4L are shown in the upper row, while results from position 4H are in the lower row. Figures 1.9(c) and 1.9(a) shows the cumulative energy distribution while figures 1.9(b) and 1.9(d) show the derivatives of these plots.

causes the shower to start earlier, and thus moves the location of the shower maximum back towards the front of the FCal. This results in a larger fraction of energy being deposited in FCal1 at position 4H compared to position 4L.

The mean response of the FCal to hadrons is plotted in figure 1.11, as a function of the beam energy. The response here is taken at the EM scale. One feature of hadronic showers is that not all of the shower's energy is visible to the calorimeter. For example, when a nucleus breaks up as a result of an interaction with a showering hadron, an amount of nuclear binding energy is lost from the products of the reaction. Alternatively, a hadronic

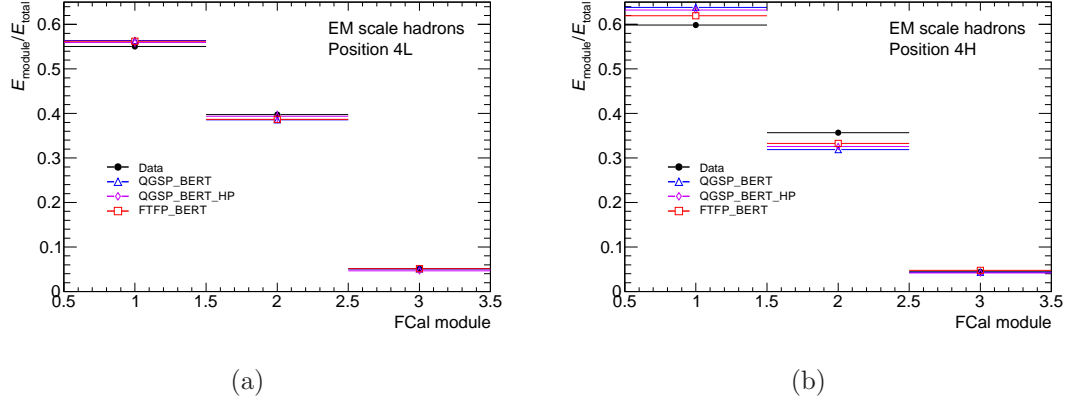


Figure 1.10: Longitudinal distributions of energy deposited in the FCal. These show the relative amounts of energy clustered in each module, for beams directed at position 4L (left) and 4H (right).

interaction may produce a neutrino, which will carry energy out of the detector. Energy lost in processes such as these cannot be measured by the calorimeter, resulting in a response lower than that of an EM particle with the same energy. For this reason, the energy reconstructed at the EM scale is only around 60-80% of the beam energies considered in this analysis. Some particles produced in hadronic interactions, such as η and π^0 mesons, decay to photons which then shower electromagnetically. Hadronic showers thus have an EM component, and the relative amount of the shower energy that is carried by this EM component increases with the energy of the initial hadron. It is this behaviour that gives rise to the non-linear shape seen in figure 1.11.

The measured energy is calibrated to the hadronic scale through a flat weighting scheme, whereby a single weight is assigned to each module. The calibrated energy is then given by

$$E_{\text{reco}} = g_1 E_1^{\text{EM}} + g_2 E_2^{\text{EM}} + g_3 E_3^{\text{EM}} \quad (1.10)$$

where E_1^{EM} , E_2^{EM} , and E_3^{EM} are the EM scale energies clustered in FCal1, FCal2 and FCal3, respectively, and g_1 , g_2 , and g_3 are the flat weights for these modules.

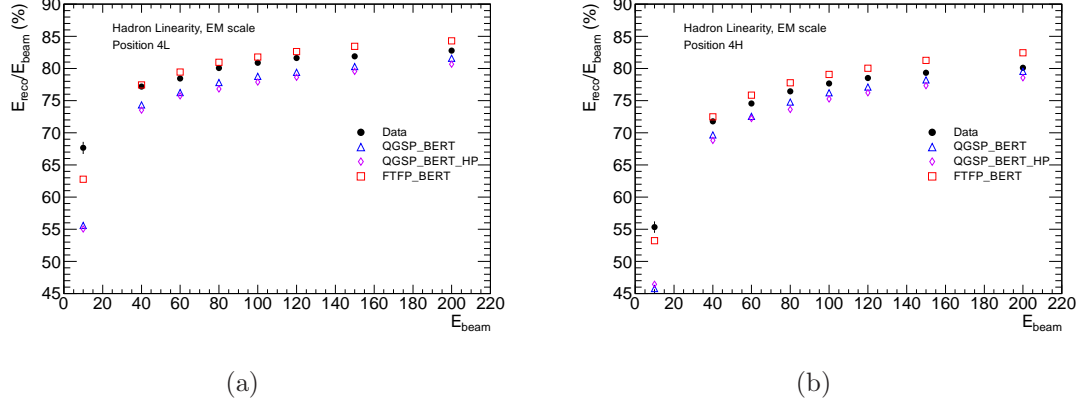


Figure 1.11: Ratio of energy reconstructed at the EM scale to the beam energy, for hadrons directed at position 4L (left) and 4H (right).

The weights are derived at a given beam energy, and are found by minimising the function

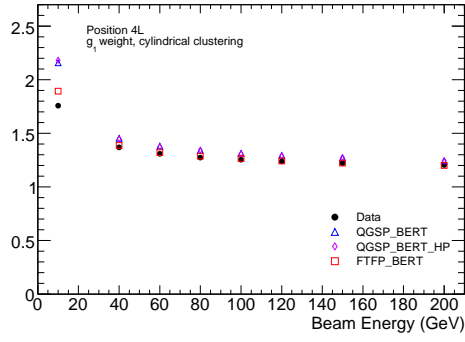
$$\chi^2 = \sum_i^{N_{\text{events}}} (g_1 E_{1,i}^{\text{EM}} + g_2 E_{2,i}^{\text{EM}} + g_3 E_{3,i}^{\text{EM}} - E_{\text{beam}})^2 \quad (1.11)$$

where E_{beam} is the beam energy and the sum over i runs over all events taken at this energy. The weights are constrained such that the mean reconstructed energy is equal to the beam energy. This constraint is implemented by assigning g_3 the value

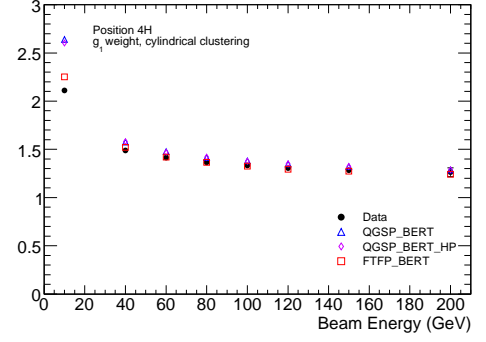
$$g_3 = \frac{E_{\text{beam}} - g_1 \langle E_1^{\text{EM}} \rangle - g_2 \langle E_2^{\text{EM}} \rangle}{\langle E_3^{\text{EM}} \rangle}, \quad (1.12)$$

where the angled brackets denote the average taken over all events. With this constraint applied, χ^2 in equation 1.11 becomes equal to the variance of the reconstructed energy, and so minimising χ^2 minimises the width of the distribution of reconstructed energy.

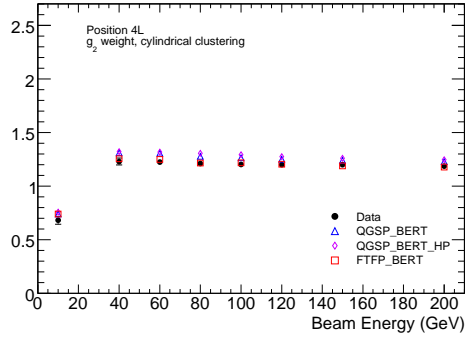
The flat weights derived at each energy are plotted in figure ???. Weights derived using Monte Carlo results are also shown for comparison, but are not used in the analysis: weights derived from 200 GeV data are used to calibrate all data and simulation results to the hadronic scale. As the beam energy decreases the relative amount of energy deposited in FCal1 and FCal2 increases, while that deposited in FCal3 decreases. At 10 GeV less energy is deposited in FCal2, and so the weight g_2 drops while g_1 rises suddenly.



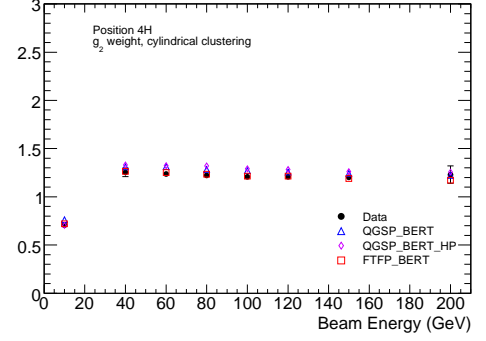
(a)



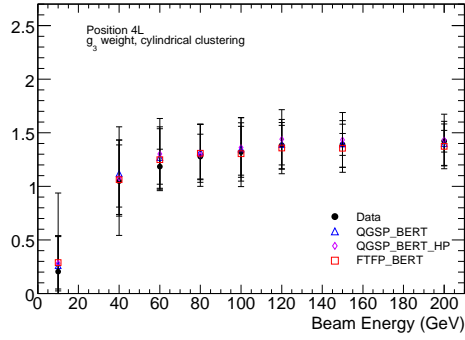
(b)



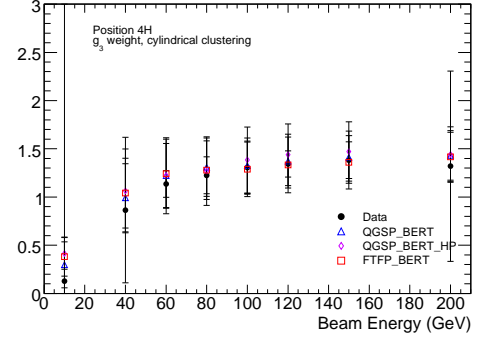
(c)



(d)



(e)



(f)

Figure 1.12: Flat weights used in hadronic calibration, as a function of the energy at which they are derived. Only the weights derived using 200GeV are used in the analysis.

The uncertainty on g_3 is found by propagating the statistical uncertainties on g_1 and g_2 . As FCal3 contains a small fraction of the total energy deposited in the FCal, even at high beam energies, this results in an uncertainty on g_3 that is much larger than the uncertainties on the other two weights.

The hadronic response of the FCal is plotted in figures 1.13 (4L) and 1.13 (4H). A double gaussian is fitted to the response and used to extract the mean and width, as was done in the electron analysis. The results obtained from the fitting are summarised in tables 1.7 and 1.8.

Beam Energy (GeV)	Fitted Mean (GeV)	Fitted Width (GeV)	Noise (GeV)
200 GeV	200.1 ± 0.1	19.5 ± 0.0	6.4 ± 0.0
150 GeV	148.4 ± 0.0	16.1 ± 0.0	6.5 ± 0.0
120 GeV	118.3 ± 0.0	14.2 ± 0.0	6.8 ± 0.0
100 GeV	97.7 ± 0.1	13.4 ± 0.1	7.3 ± 0.0
80 GeV	77.3 ± 0.1	11.3 ± 0.0	6.5 ± 0.0
60 GeV	56.7 ± 0.0	9.6 ± 0.0	6.1 ± 0.0
40 GeV	37.2 ± 0.1	8.5 ± 0.1	6.1 ± 0.0
10 GeV	8.2 ± 0.1	6.6 ± 0.1	6.2 ± 0.1

Table 1.7: Results for the FCal response to hadrons directed at position 4L. Quoted errors are statistical only.

Beam Energy (GeV)	Fitted Mean (GeV)	Fitted Width (GeV)	Noise (GeV)
200 GeV	201.0 ± 0.1	23.4 ± 0.0	6.5 ± 0.0
150 GeV	149.5 ± 0.1	19.1 ± 0.1	6.4 ± 0.0
120 GeV	118.4 ± 0.1	17.1 ± 0.0	7.2 ± 0.0
100 GeV	97.5 ± 0.1	15.9 ± 0.1	7.6 ± 0.0
80 GeV	76.7 ± 0.1	14.1 ± 0.0	7.6 ± 0.0
60 GeV	56.1 ± 0.0	11.7 ± 0.0	6.7 ± 0.0
40 GeV	36.1 ± 0.1	9.9 ± 0.1	6.5 ± 0.1
10 GeV	7.0 ± 0.1	7.2 ± 0.1	6.4 ± 0.1

Table 1.8: Results for the FCal response to hadrons directed at position 4H. Quoted errors are statistical only.

The ratio of mean reconstructed energy at the hadronic scale to the beam energy is plotted in figure 1.15. As most of the energy is deposited in FCal1 and FCal2, which

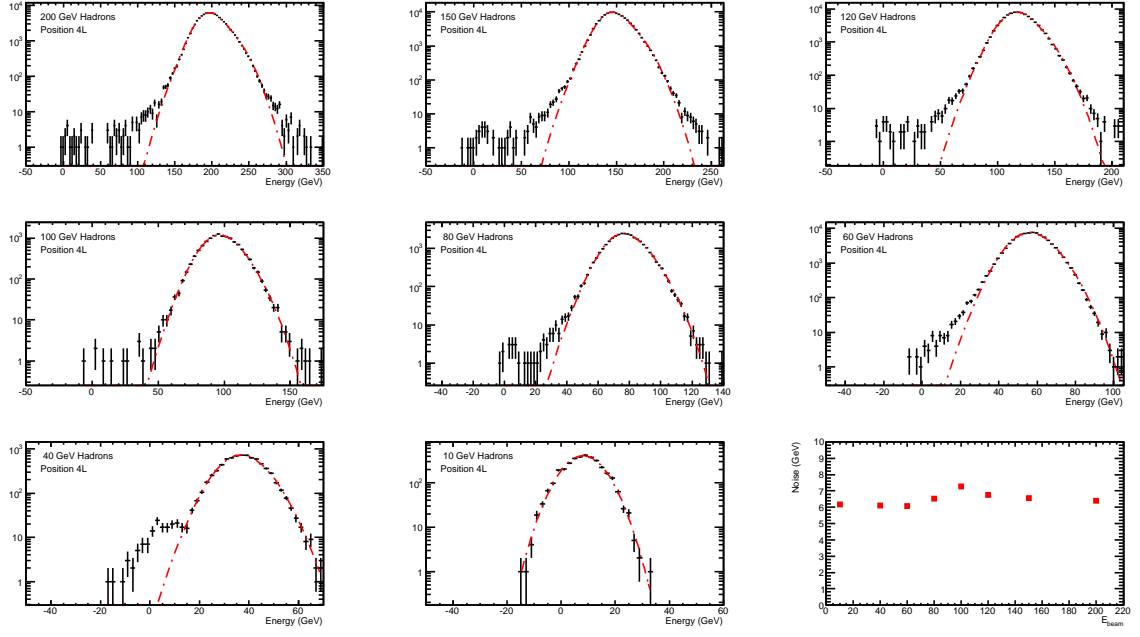


Figure 1.13: FCal response to hadron beams directed at position 4L. The lower-right plot shows the clustered noise (in GeV) at each energy.

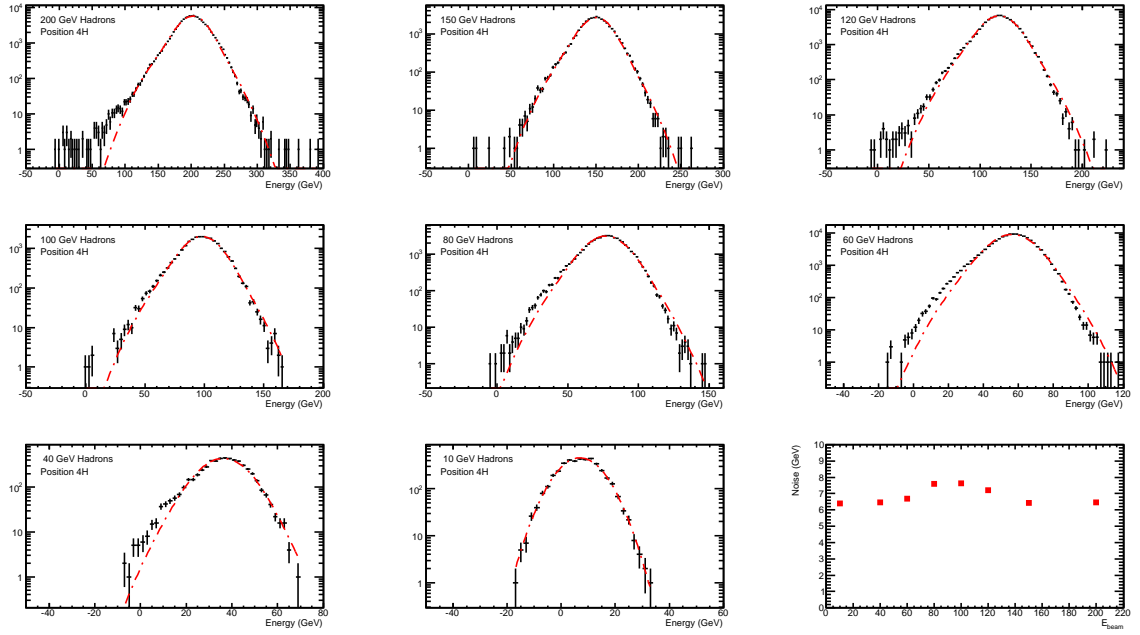


Figure 1.14: FCal response to hadron beams directed at position 4H. The lower-right plot shows the clustered noise (in GeV) at each energy.

have similarly valued weights at 200 GeV, the shape of these plots are very similar to those shown in figure 1.11.

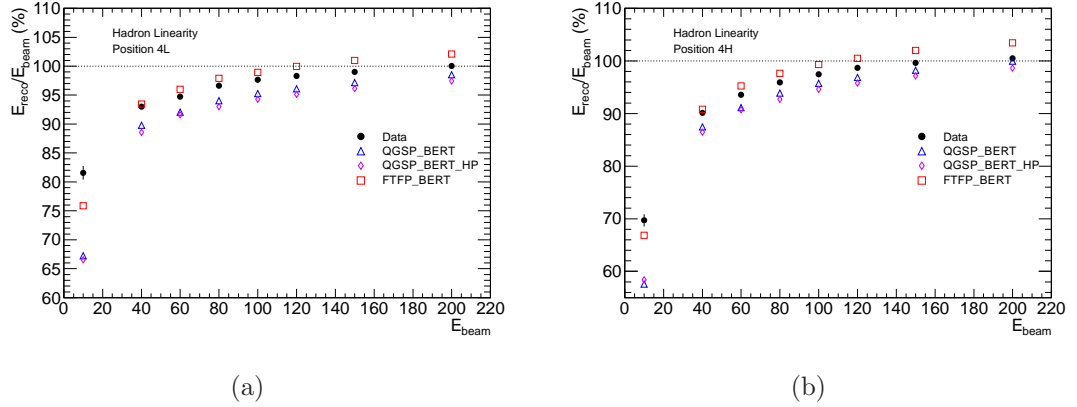


Figure 1.15: Ratio of reconstructed energy to beam energy for hadrons directed at position 4L (left) and 4H (right). Hadronic calibration is accomplished through flat weights, which are derived from the 200GeV data.

The energy resolution of the FCal to hadrons is plotted in figure 1.16. At higher energies the data and simulation results agree to within a 1-2% percent. The resolution information is fit to the same function used for electrons; the results of which are listed in table 1.9.

Systematic effects on the resolution are dominated by the choice of weights used for hadronic calibration. The weights derived at 100GeV, 120GeV and 150 GeV are used to estimate this uncertainty. Each set of weights is used to calibrate the data and obtain information on the resolution, which is then fit. The largest deviation seen between the fits obtained using these weights and the nominal set of weights (which are derived at 200 GeV) is then taken as the systematic uncertainty. Uncertainties related to the fitting procedure, histogram binning and event selection criteria are also considered, with uncertainties arising from different sources being summed in quadrature. The values for the stochastic and constant term of the resolution at position 4L are thus $88 \pm 3\%$ $\text{GeV}^{1/2}$ and $6.8 \pm 0.4\%$, respectively, where the quoted uncertainties are systematic. For position 4H, the stochastic and constant term are $121 \pm 7\%$ $\text{GeV}^{1/2}$ and $7.1 \pm 1.2\%$,

respectively.

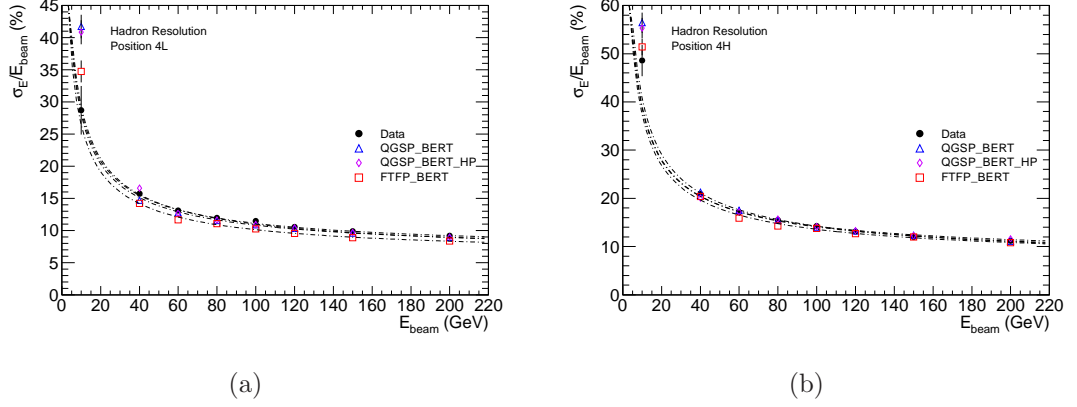


Figure 1.16: Energy resolution of the FCal to hadrons, using data taken from position 4L (left) and 4H (right). A noise subtraction procedure has been applied, as described in the text.

	Stochastic Term (% $\text{GeV}^{1/2}$)	Constant Term (%)
Data (4L)	88.0 ± 0.6	6.79 ± 0.06
QGSP_BERT (4L)	86.2 ± 1.1	6.54 ± 0.18
QGSP_BERT_HP (4L)	90.5 ± 1.1	6.22 ± 0.13
FTFP_BERT (4L)	81.2 ± 1.1	6.04 ± 0.11
Data (4H)	121.3 ± 0.6	7.13 ± 0.07
QGSP_BERT (4H)	127.2 ± 1.1	6.41 ± 0.17
QGSP_BERT_HP (4H)	119.6 ± 1.2	7.71 ± 0.15
FTFP_BERT (4H)	115.8 ± 1.1	7.12 ± 0.14

Table 1.9: Fit parameters for energy resolution to electrons. Quoted uncertainties are statistical only.

1.3 Topologically Clustered Results

1.3.1 Electrons

In addition to cylindrical clusters, topological clusters (as described in section ??) are formed during the reconstruction of each event. The clustering is done in **Athena** using the standard "420" thresholds. The noise values used to define these thresholds are obtained from randomly triggered data. In **ATLAS**, the tracking detectors do not cover the pseudorapidity region in which the FCal is located. Topological clusters do not require tracking information for their formation, and thus they can be used to measure energy deposited in the FCal during data taking at the LHC.

The topoclustering software in **Athena** contains a splitting step [?], which is enabled by default. The splitter is intended to form new cluster within existing clusters, in cases where the new clusters can be associated with energy deposited by individual particles. New clusters are formed around local maxima, which are cells that satisfy the following conditions:

- have more energy than any adjacent cells
- have at least 4 neighboring cells belonging to the original cluster
- have energy greater than 500 MeV

As the RMS of the noise in the hadronic modules of the FCal is close to 500 MeV, the splitter has been turned off in this analysis in order to prevent noise fluctuations from creating new clusters.

The response of the FCal to electrons is shown in figures 1.17 and 1.17, for beams directed at position 4L and 4H respectively. As with the cylindrically results, the response is fit to the sum of a double gaussian (for the electron peak) and an contribution derived from hadron data in order to account for any residual beam contamination. Quantities obtained from the fit are listed in tables 1.10 and 1.11

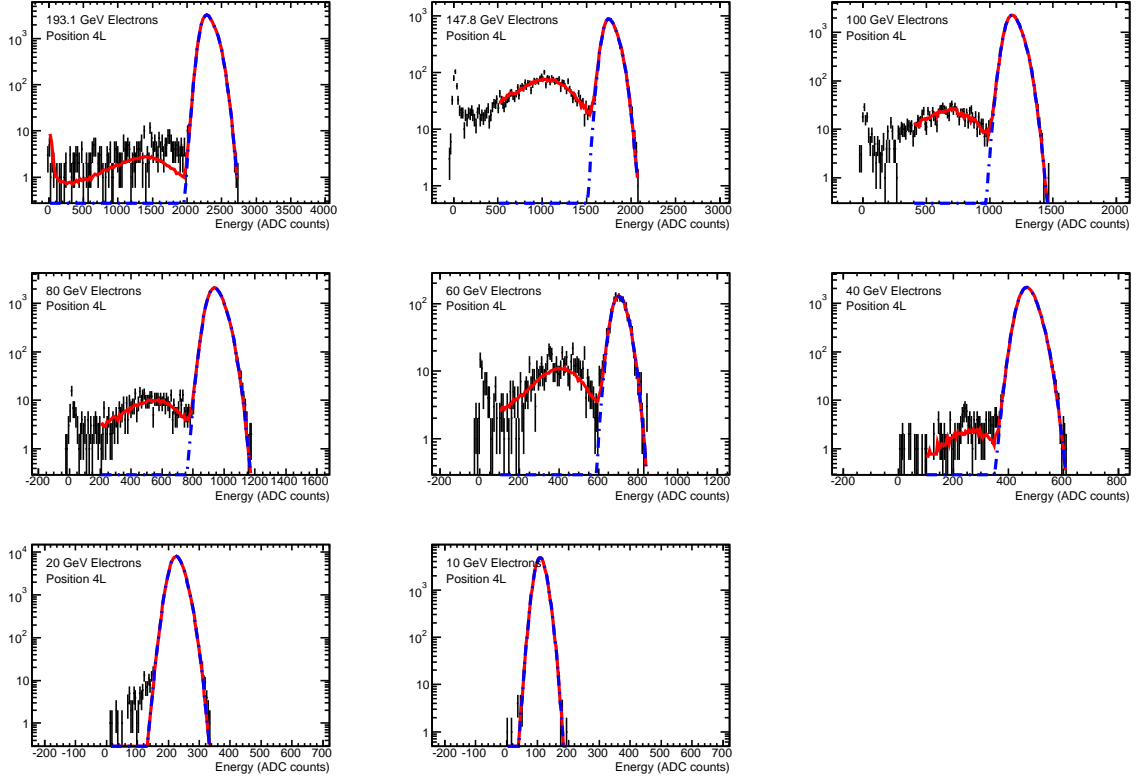


Figure 1.17: FCal response to electron beams directed at position 4L. The lower-right plot shows the clustered noise (in GeV) at each energy.

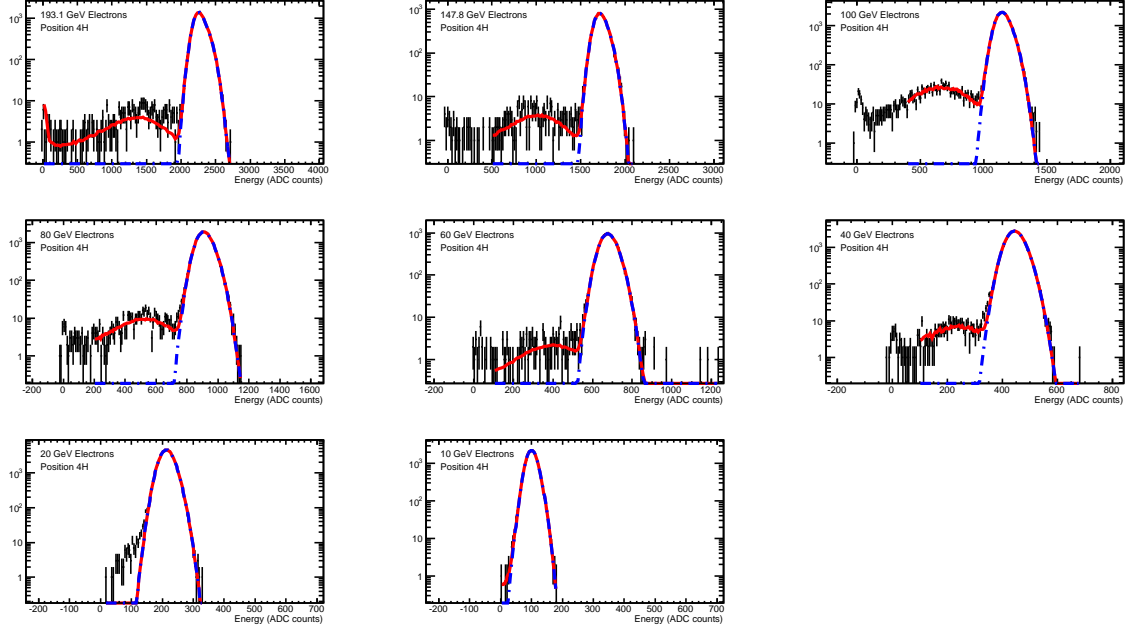


Figure 1.18: FCal response to electron beams directed at position 4H, .

Beam Energy (GeV)	Fitted Mean (ADC)	Fitted Width (ADC)	Noise (ADC)
193.1 GeV	2312.4 ± 0.5	95.4 ± 0.3	18.8 ± 0.1
147.8 GeV	1769.8 ± 0.8	77.5 ± 0.5	21.6 ± 0.1
100 GeV	1189.3 ± 0.3	58.0 ± 0.2	19.7 ± 0.1
80 GeV	948.1 ± 0.3	49.2 ± 0.2	18.6 ± 0.1
60 GeV	707.9 ± 1.0	37.0 ± 0.7	15.3 ± 0.2
40 GeV	471.2 ± 0.2	30.2 ± 0.1	14.1 ± 0.1
20 GeV	227.8 ± 0.1	20.9 ± 0.1	12.7 ± 0.0
10 GeV	109.6 ± 0.1	15.9 ± 0.1	11.5 ± 0.0

Table 1.10: Results for the FCal response to electrons, using topologically clustered data from beams directed at position 4L. Quoted uncertainties are statistical only.

The linearity obtained using topological clusters is shown in figure 1.19. The slopes obtained from the topologically clustered results are marginally higher than those obtained from cylindrical clustering, while the intercepts are slightly lower. Cells containing low amounts of energy may not be included in the topoclusters in cases where they would be included in a cylindrical cluster, giving the topoclusters a lower energy than the cylindrical clusters. This effect would be more significant at low energies than high energies,

Beam Energy (GeV)	Fitted Mean (ADC)	Fitted Width (ADC)	Noise (ADC)
193.1 GeV	2278.5 ± 0.7	91.9 ± 0.5	20.8 ± 0.1
147.8 GeV	1726.5 ± 0.8	73.2 ± 0.5	19.5 ± 0.1
100 GeV	1154.2 ± 0.3	56.5 ± 0.2	19.8 ± 0.1
80 GeV	913.8 ± 0.3	50.0 ± 0.2	18.7 ± 0.1
60 GeV	680.4 ± 0.4	41.1 ± 0.3	16.8 ± 0.1
40 GeV	446.9 ± 0.2	31.2 ± 0.1	14.8 ± 0.1
20 GeV	214.6 ± 0.1	22.1 ± 0.1	13.1 ± 0.0
10 GeV	101.2 ± 0.1	17.0 ± 0.1	11.6 ± 0.1

Table 1.11: Results for the FCal response to electrons, using topologically clustered data from beams directed at position 4H. Quoted uncertainties are statistical only.

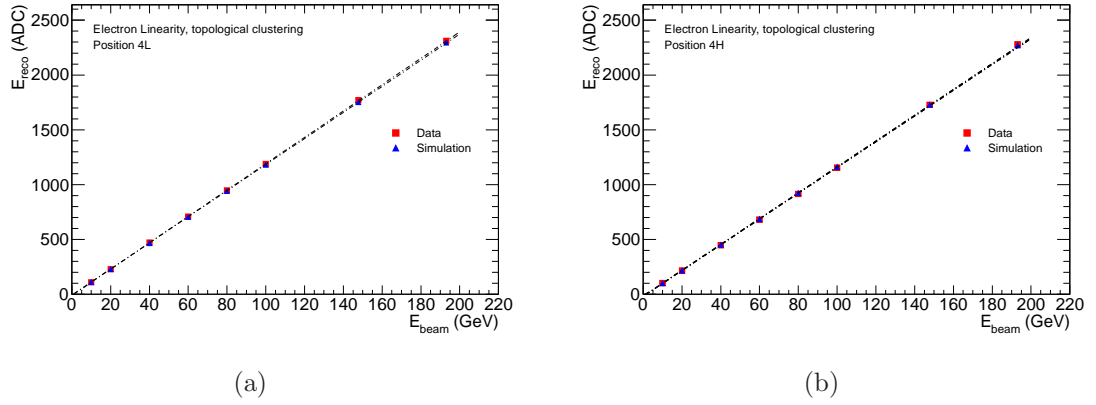


Figure 1.19: Ratio of reconstructed energy to the beam energy, for electrons directed at position 4L (left) and 4H (right).

and may explain the lower intercept and higher slope seen in the topoclustered results.

Systematics are estimated using the same method employed in the case for cylindrical clustering. To estimate the effect of the clustering method, a "430" clustering scheme was also used and compared with the results of the "420" method. The slope and intercept for topoclustered data at position 4L are 12.02 ± 0.04 GeV/ADC and -11.7 ± 1.2 ADC counts, respectively, where the quoted uncertainties are systematic. At position 4H, the slope is 11.75 ± 0.6 GeV/ADC and the intercept is -19.9 ± 2.3 ADC counts.

The energy resolution is plotted in figure 1.20, with fit results listed in table 1.13. The noise subtraction procedure is done in the same way as it was for the cylindrically

linearity result	slope (ADC/GeV)	Intercept (ADC)
Data (4L)	12.023 ± 0.002	-11.67 ± 0.07
Simulation (4L)	11.905 ± 0.003	-7.96 ± 0.12
Data (4H)	11.751 ± 0.002	-19.86 ± 0.09
Simulation (4H)	11.789 ± 0.003	-16.74 ± 0.12

Table 1.12: Linearity results for electron data. quoted uncertainties are statistical.

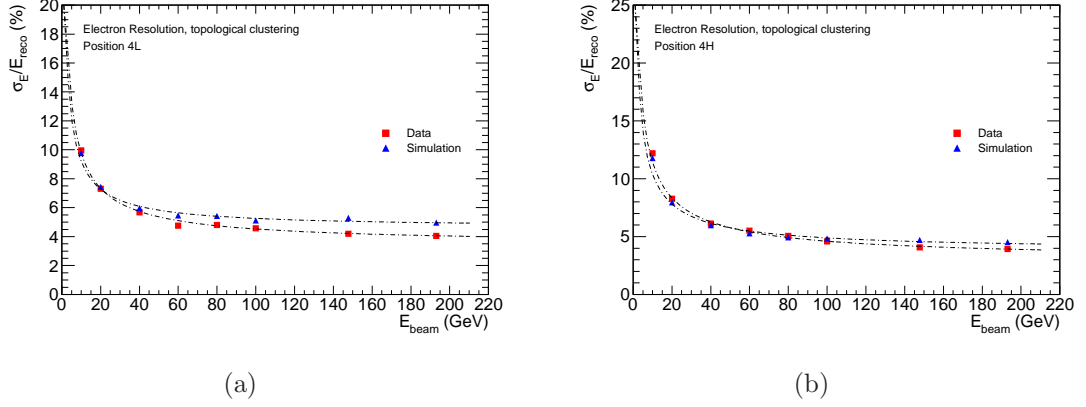


Figure 1.20: Energy resolution of the FCal to electrons directed at position 4L (left and position 4H (right).

clustered case. As cells with low energy are not included in the topological clusters, this reduces the number of cells sampled and causes a slight increase in the stochastic term compared to the case for cylindrical clustering.

	Stochastic Term (% $\text{GeV}^{1/2}$)	Constant Term (%)
Data (4L)	28.8 ± 0.1	3.49 ± 0.02
Simulation (4L)	25.2 ± 0.3	4.62 ± 0.02
Data (4H)	34.8 ± 0.2	3.02 ± 0.03
Simulation (4H)	30.5 ± 0.3	3.82 ± 0.03

Table 1.13: Fit parameters for energy resolution to electrons. Quoted uncertainties are statistical only.

1.3.2 Hadrons

The ratio of the mean response (at the EM scale) to the beam energy is plotted in figure ??, for hadron events that have been clustered topologically. These plots exhibit

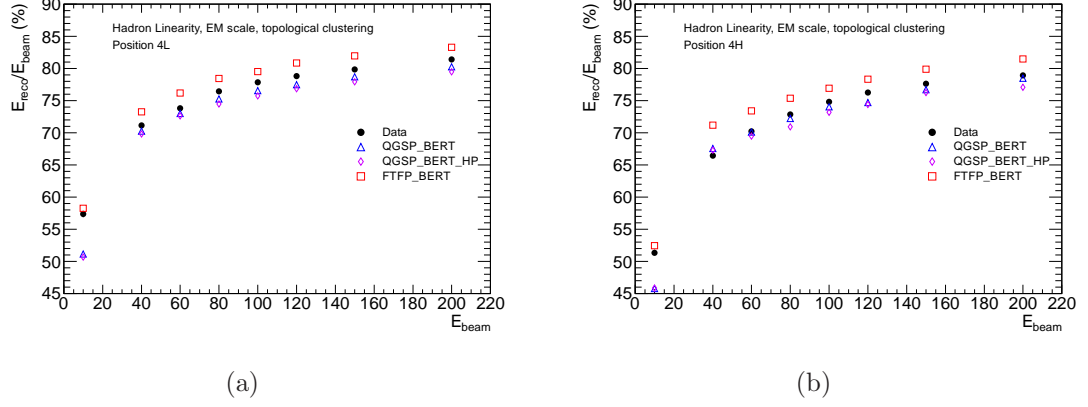


Figure 1.21: Ratio of energy reconstructed at the EM scale to the beam energy, for hadrons directed at position 4L (left) and 4H (right).

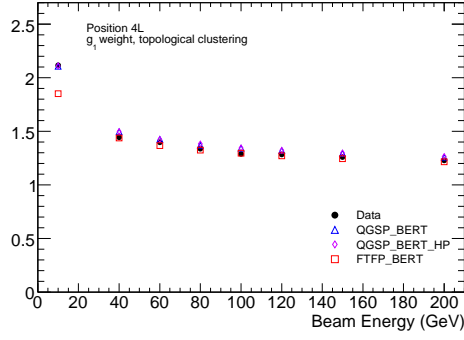
Beam Energy (GeV)	Fitted Mean (GeV)	Fitted Width (GeV)	Noise (GeV)
200 GeV	200.1 ± 0.1	19.6 ± 0.0	5.1 ± 0.0
150 GeV	147.1 ± 0.0	16.0 ± 0.0	4.7 ± 0.0
120 GeV	116.1 ± 0.1	13.9 ± 0.0	4.3 ± 0.0
100 GeV	95.6 ± 0.1	13.0 ± 0.1	4.8 ± 0.0
80 GeV	75.1 ± 0.1	11.0 ± 0.0	4.1 ± 0.0
60 GeV	54.3 ± 0.0	9.1 ± 0.0	3.6 ± 0.0
40 GeV	34.9 ± 0.1	7.6 ± 0.1	3.1 ± 0.0
10 GeV	7.0 ± 0.1	3.3 ± 0.0	1.9 ± 0.0

Table 1.14: FCal response to hadrons at position 4L, obtained from fits to topologically clustered data.

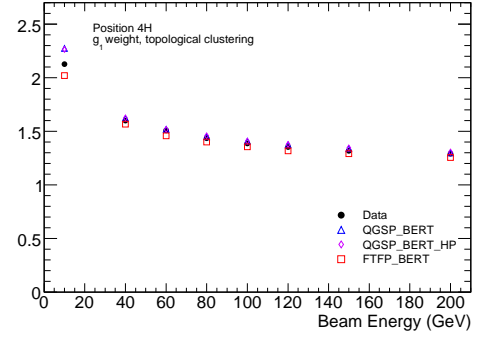
the same behaviour seen for cylindrical clustering, although there is better agreement between data and simulation at lower energies. The weights used for hadronic calibration are derived in the same way, and are plotted in figure ?? . At high energy, the weights are very similar to those obtained with cylindrical clusters. At lower energies less energy is contained within the topological clustering, and so the derived weights in FCal1 and FCal2 are much larger than for the cylindrically clustered case.

The calibrated responses are plotted in figures 1.23 and ?? and summarised in tables 1.14 and 1.15. While the mean response is slightly diminished, the clustered noise is significantly lower due to the noise reducing properties of the topological clustering.

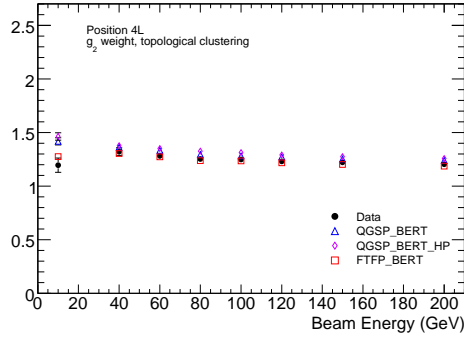
The mean response (hadronically calibrated) is plotted in figure 1.25 as a function



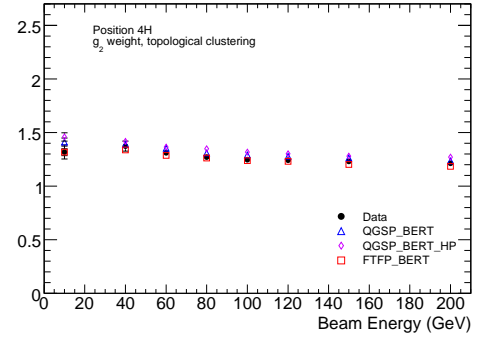
(a)



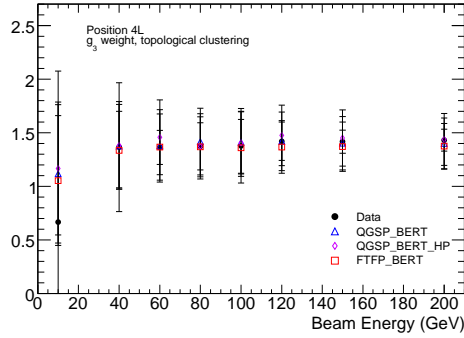
(b)



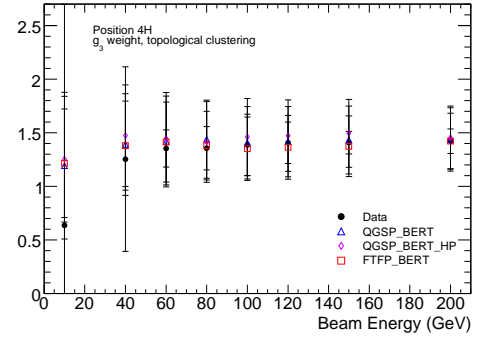
(c)



(d)



(e)



(f)

Figure 1.22: Flat weights used in hadronic calibration, as a function of the energy at which they are derived. Only the weights derived using 200GeV are used in the analysis.

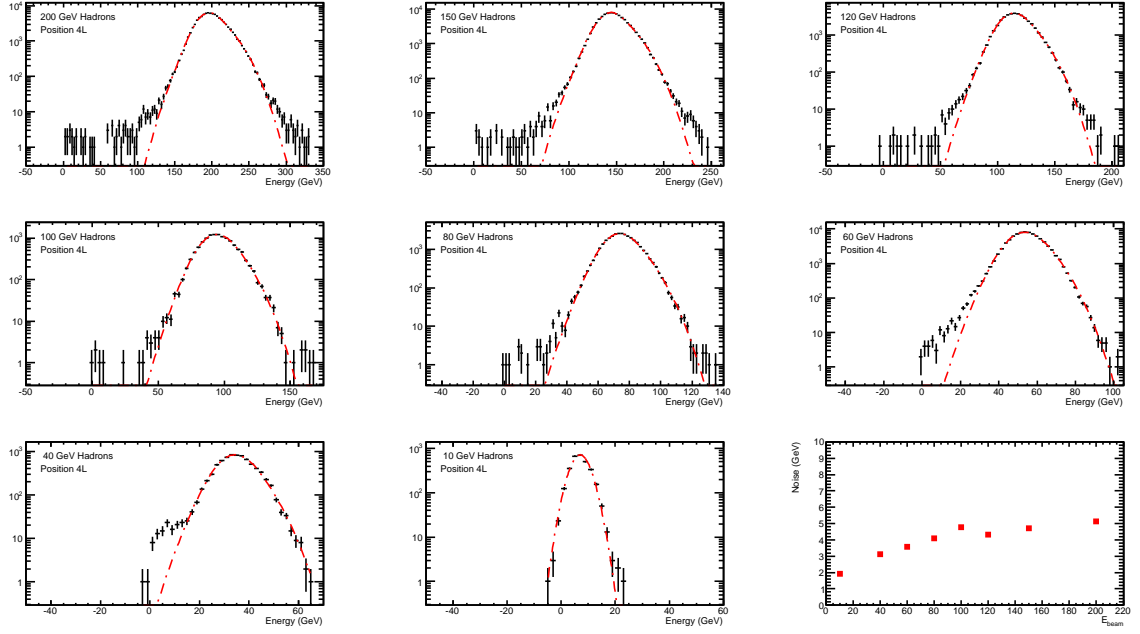


Figure 1.23: FCal response to hadron beams directed at position 4L.

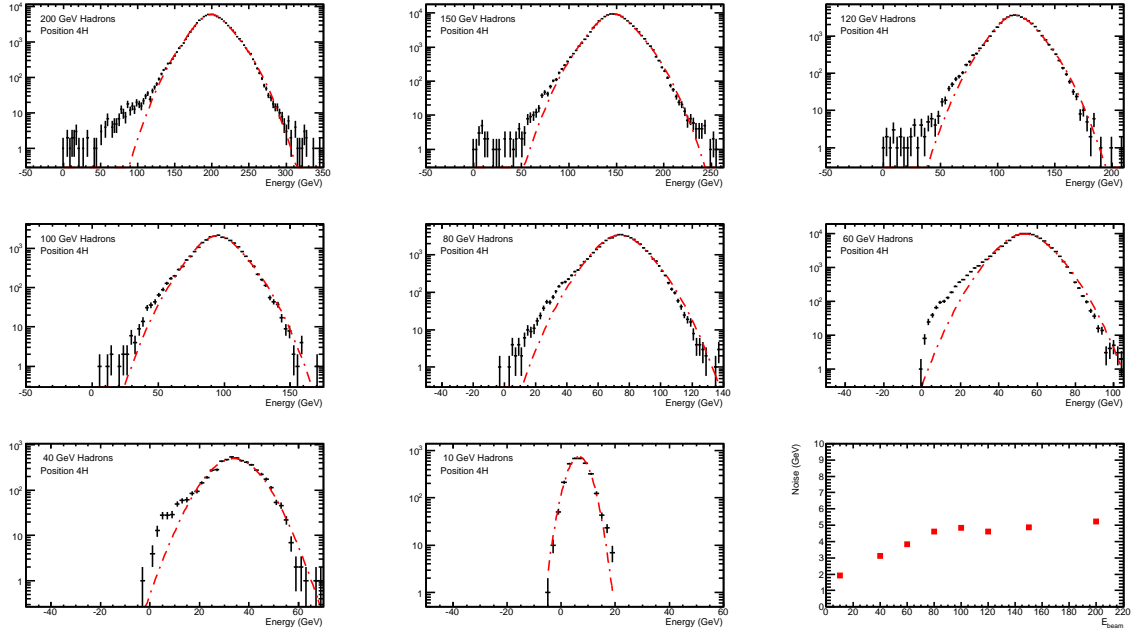


Figure 1.24: FCal response to hadron beams directed at position 4H.

of beam energy. Again, as most of the energy is deposited in FCal1 and FCal2, which have similar weights, the shape of this plot is very similar to that seen at the EM scale

Beam Energy (GeV)	Fitted Mean (GeV)	Fitted Width (GeV)	Noise (GeV)
200 GeV	200.2 ± 0.1	22.5 ± 0.0	5.2 ± 0.0
150 GeV	147.5 ± 0.0	18.6 ± 0.0	4.9 ± 0.0
120 GeV	116.0 ± 0.1	16.1 ± 0.1	4.6 ± 0.0
100 GeV	95.0 ± 0.1	15.2 ± 0.1	4.9 ± 0.0
80 GeV	74.0 ± 0.1	13.3 ± 0.0	4.6 ± 0.0
60 GeV	53.5 ± 0.0	10.8 ± 0.0	3.8 ± 0.0
40 GeV	33.8 ± 0.1	8.6 ± 0.1	3.1 ± 0.0
10 GeV	6.5 ± 0.1	3.4 ± 0.0	1.9 ± 0.0

Table 1.15: FCal response to hadrons at position 4H, obtained from fits to topologically clustered data.

in figure 1.21. While the topological clustering had only a slight effect on the linearity for electrons, the energy density in hadronic showers is much lower, and so the topological clustering excludes a significantly larger fraction of the energy. This results in the mean response being considerably lower at energies below 200GeV when compared to the cylindrically clustered case.

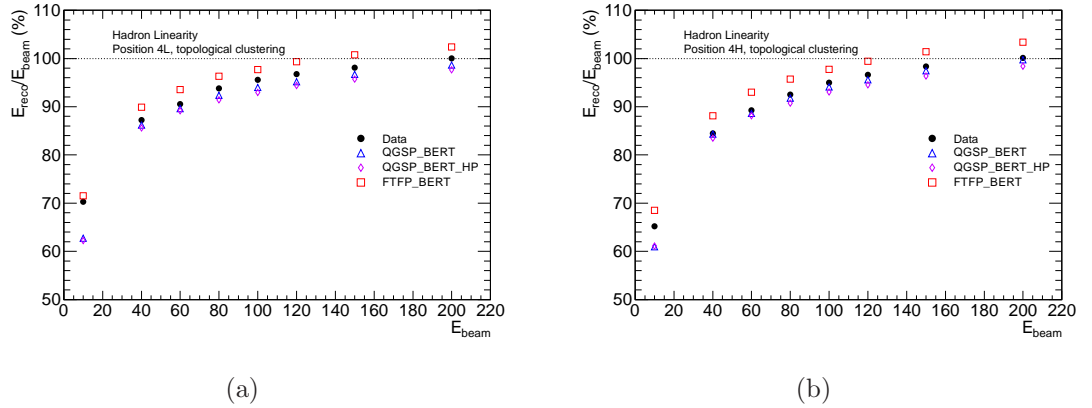


Figure 1.25: Ratio of reconstructed energy to the beam energy, for hadrons directed at position 4L (left) and 4H (right). Flat weights have been applied to calibrate the reconstructed energy to the hadronic scale.

The resolution is plotted in figure 1.26, and fit results are listed in table 1.16. Again, as less energy is included in the topological clusters the stochastic term is substantially increased compared to the resolutions obtained from cylindrical clustering. The stochastic terms increase by $\sim 20\% \text{GeV}^{1/2}$ at position 4L and by 10-20 $\% \text{GeV}^{1/2}$ at position 4H. In

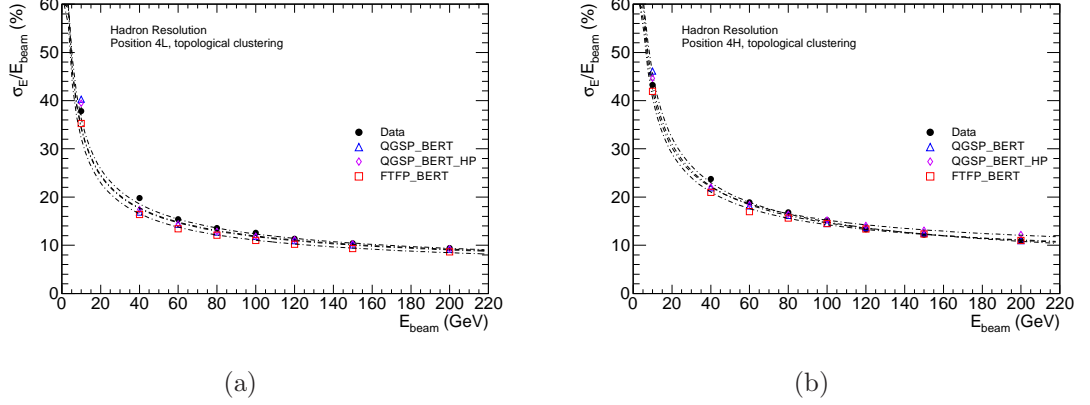


Figure 1.26: Energy resolution of the FCal to hadrons directed at position 4L (left and position 4H (right). Flat weights have been applied to calibrate the reconstructed energy to the hadronic scale.

spite of this large increase in the stochastic term, the resolution at 200GeV is relatively unchanged. Systematic effects on the resolution are again dominated by the hadronic weights, giving values of $114 \pm 2\% \text{ GeV}^{1/2}$ for the stochastic term and $4.9 \pm 0.3\%$ for the constant term at position 4L. At position 4H the stochastic term is $137 \pm 6\% \text{ GeV}^{1/2}$ while the constant term is $3.8 \pm 1.3\%$.

	Stochastic Term ($\% \text{ GeV}^{1/2}$)	Constant Term (%)
Data (4L)	113.5 ± 0.4	4.86 ± 0.08
QGSP_BERT (4L)	107.0 ± 0.7	4.97 ± 0.12
QGSP_BERT_HP (4L)	107.6 ± 0.7	5.18 ± 0.12
FTFP_BERT (4L)	100.7 ± 0.6	4.59 ± 0.12
Data (4H)	143.6 ± 0.4	3.80 ± 0.12
QGSP_BERT (4H)	136.6 ± 0.8	5.30 ± 0.17
QGSP_BERT_HP (4H)	130.1 ± 0.8	7.77 ± 0.12
FTFP_BERT (4H)	126.4 ± 0.7	6.62 ± 0.13

Table 1.16: Fit parameters for energy resolution to hadrons, obtained using topologically clustered data. Quoted uncertainties are statistical only.

1.3.3 Cluster moments

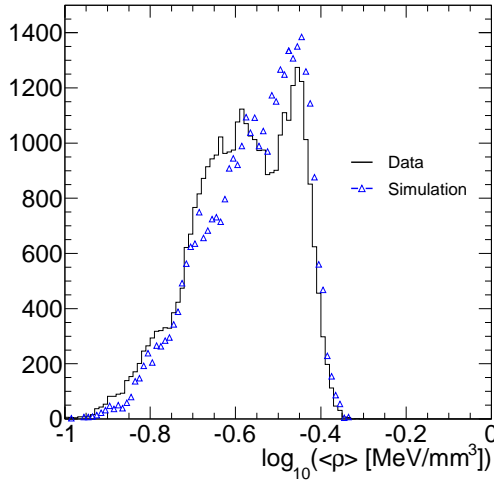
reference the nim paper, compare our results to theirs (generally agree) Local Hadronic Calibration is another method for calibrating energy deposits to the hadronic scale. This

method is applied to topological clusters, and makes use of various moments that describe the shape of the energy deposit. These moments are used to classify a cluster as being electromagnetic or hadronic in nature, and the cluster is then weighted appropriately. Two of the most important of these moments are the energy density, ρ , and λ_c , which describes the depth of the energy deposit within the calorimeter.

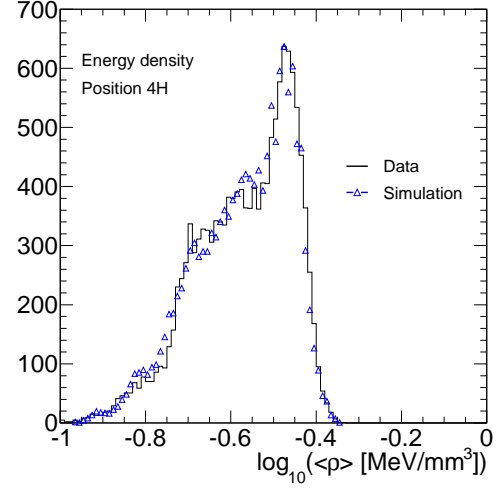
These moments are plotted in figure 1.27 for electrons and figure 1.28 for hadrons. The data and simulation are generally in agreement for the electron results, however the simulation results for the cluster depth have a tail at high λ_c which is significantly enhanced compared to that seen in data.

For hadrons, the data and simulation agree quite well. The simulation results for the energy density are a little higher than that seen in data, while for the cluster depth the simulation results are a little lower. These results are expected given that the simulation generates showers that are shorter and narrower than those seen in data (c.f. figures 1.10 and 1.9).

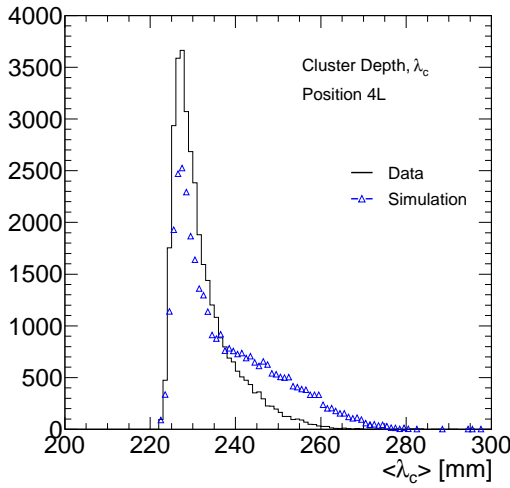
s in MeV



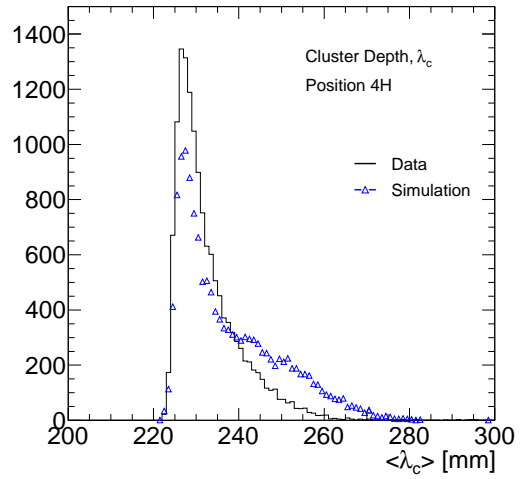
(a)



(b)

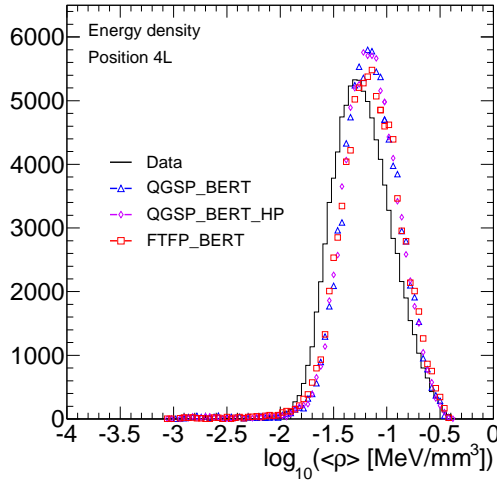


(c)

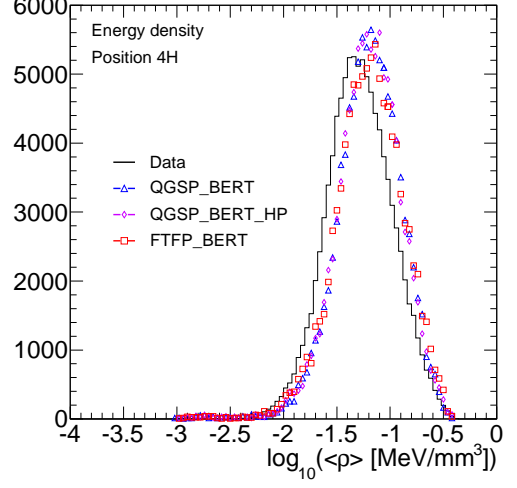


(d)

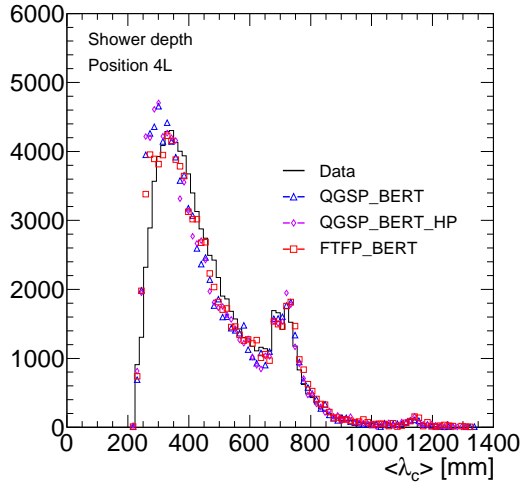
Figure 1.27: Shower moments derived from topological clusters. The upper plots show the energy density of clusters resulting from 193GeV electrons directed at position 4L (left) and 4H (right). The lower plots show the distribution of λ_c , which describes the depth of the cluster centre within the calorimeter.



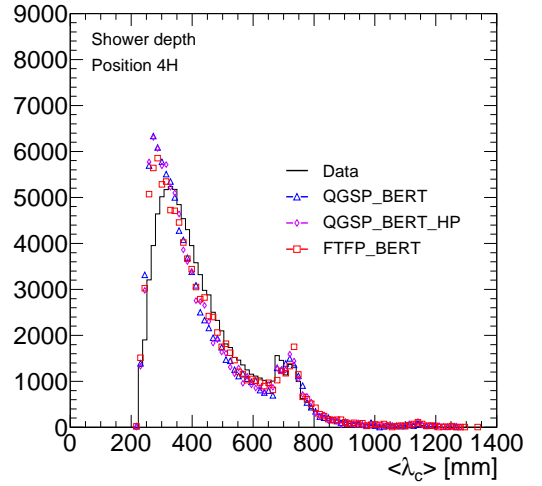
(a)



(b)



(c)



(d)

Figure 1.28: Shower moments derived from topological clusters. The upper plots show the energy density of clusters resulting from 200GeV hadrons directed at position 4L (left) and 4H (right). The lower plots show the distribution of λ_c , which describes the depth of the cluster centre within the calorimeter.

Bibliography

- [1] J. P. Archambault et al. Energy calibration of the ATLAS liquid argon forward calorimeter. *JINST*, 3:P02002, 2008.
- [2] W Lampl, S Laplace, D Lelas, P Loch, H Ma, S Menke, S Rajagopalan, D Rousseau, S Snyder, and G Unal. Calorimeter clustering algorithms: Description and performance. (ATL-LARG-PUB-2008-002. ATL-COM-LARG-2008-003), Apr 2008.